npj | Clean Water

www.nature.com/npjcleanwater

ARTICLE OPEN

Check for updates

Rheologically controlled design of nature-inspired superhydrophobic and self-cleaning membranes for clean water production

Kang Jia Lu[1], Dieling Zhao[1], Yuanmiaoliang Chen[2], Jian Chang[3] and Tai-Shung Chung[1,2]✉

Conventional fabrication technologies of superhydrophobic and self-cleaning membranes for wastewater treatment often involve complex surface modifications, and massive usage of nanomaterials or organic solvents. In this work, we developed a pure rheological spray-assisted nonsolvent induced phase separation (SANIPS) approach to fabricate self-cleaning polyvinylidene fluoride (PVDF) membranes with high porosity and hierarchical micro/nanostructures. The resultant membranes exhibit water contact angles and sliding angles in the range of 151.9–156.2° and 9.6–22.6°, respectively. We found that the spraying step caused local distortion of the membrane surface and induced a two-stage phase inversion, leading to the formation of multilevel polymeric crystal structures. Moreover, the morphological structures and other membrane properties (e.g., mechanical strength and liquid entry pressure) could be tuned by applying spraying materials with different physicochemical properties. The superior anti-wetting and self-cleaning properties of the resultant membranes have been demonstrated by treating hypersaline wastewater, comprising 10% sodium chloride and 2000 p.p.m. Rose Bengal dye via direct contact membrane distillation (DCMD) tests. The SANIPS membrane showed a remarkably stable vapor flux of 36.0 kg m^{-2} h at a feed temperature of 60 °C, and a salt rejection over 99.9% throughout the long-term test of 100 h. We envision this facile and green fabrication method will pave the way for large-scale production of superhydrophobic and self-cleaning membranes for diverse water treatment processes.

npj Clean Water (2020)3:30 ; https://doi.org/10.1038/s41545-020-0078-2

INTRODUCTION

Inspirations from natural nonwetting surfaces have stimulated the rapid development of superhydrophobic and self-cleaning surfaces in the past two decades[1]. In recent years, the membranes with water contact angles over 150° and sliding angles <10°, have drawn increasing attention in the field of wastewater treatment because of their remarkable water resistance, high rejection, low fouling tendency, and good long-term stability[2–5]. For example, membranes with superhydrophobic–superoleophilic properties have been reported to be effective in separating water from oil by either filtration or absorption methods[6–8]. Superhydrophobic membranes have also been employed as a liquid barrier and a contact surface for water evaporation in membrane distillation (MD), where water vapor generated from the hot feed stream permeates through the hydrophobic porous membrane, and gets condensed and collected by the cold distillate stream[9–14].

Intensive investigations on natural superhydrophobic surfaces, such as lotus or taro leaves reveal that a stable liquid–vapor–solid composite interface formed on low-surface-energy hierarchical structures is the key to achieve superior water repellence and self-cleaning properties[15,16]. Inspired by nature, many artificial highly hydrophobic membranes developed in recent years combine modifications with greater surface roughness and lower surface energy as summarized in Table 1. Depositing nanomaterials, such as TiO_2 nanoparticles or carbon nanotubes on polymeric substrates has been the most common method to mimic hierarchical surface structures[1,17–20]. However, grafting a uniform layer of nanomaterials on polymeric substrates can be time consuming and chemically intensive because most hydrophobic polymers, such as polyvinylidene difluoride (PVDF), polypropylene, and polytetrafluoroethylene are chemically inert. Moreover, the risk of leaching these nanomaterials becomes a growing concern due to their potential toxicity to both human beings and environments[21]. Alternative ways of creating porous and rough surface structures are through delayed nonsolvent induced phase separation (NIPS) or vapor induced phase separation (VIPS)[22–24]. In a NIPS process, a polymer solution is cast on a flat plate and then immersed in a nonsolvent coagulant bath, where phase inversion takes place due to the exchange between solvents in the nascent membrane and nonsolvents in the coagulation bath[12]. If a soft coagulant bath containing a certain percentage of alcohols[24–26], *N*-*N*-dimethylacetamide (DMAc)[22], or triethyl phosphate (TEP)[27] was employed, phase inversion will be retarded both thermodynamically and kinetically. The delayed phase inversion allows polymer crystals to grow into larger sizes, and thus significantly enhances the membrane roughness and water contact angles[25]. Nevertheless, the massive use of organic solvents increases the cost and carbon footprint. In a VIPS process, the newly cast membrane is exposed to humid air for a fixed duration, which allows a formation of a partially solidified top surface in air due to moisture condensation[28]. After being immersed in the coagulant, the newly formed skin impedes the phase inversion rate, and thus facilitates the growth of polymer crystals. Nevertheless, it often takes a prolonged exposure time in order to achieve the desirable surface roughness. Moreover, contact angle hysteresis or sliding angle is rarely reported in these studies. Electrospinning is another alternative way of fabricating highly porous membranes with complex hierarchical structures[8,14,20,29,30]. However, most of the

[1]Chemical and Biomolecular Engineering, National University of Singapore, Singapore 117576, Singapore. [2]NUS Graduate School for Integrative Science and Engineering, National University of Singapore, Singapore 117456, Singapore. [3]Chemical and Biomolecular Engineering, University of Pennsylvania, 220 South 33rd Street, Philadelphia, PA USA 19104, USA. ✉email: chencts@nus.edu.sg

Published in partnership with King Fahd University of Petroleum & Minerals

npj nature partner journals

Table 1. A survey of highly hydrophobic membranes, and their fabrication and modification methods.

Refs.	Base membranes	Fabrication methods of base membranes	Surface modification methods	Contact/sliding angles (°)	Applications
[18]	PVDF flat sheet membrane	N.A. (commercial)	TiO_2 deposition followed by 1H, 1H, 2H, 2H-perfluorododecyltrichlorosilane coating	CA: 163°; SA: N.A.	DCMD
[5]	Ceramic membrane	Coating a ZrO_2 membrane layer on an alumina support	Grafting with fluoroalkylsilane	CA: 153°; SA: N.A.	CO_2 capture
[4]	ZIF-8/PDMS membrane	Dip coating	UV/ozone treatment followed by deposition of semifluorinated molecules	CA: 152.4°; SA: ~7°	Bioalcohol pervaporation
[24]	PVDF flat sheet membrane	NIPS method with alcohol coagulants	No	CA: 144–148°; SA: N.A.	DCMD
[22]	PVDF flat sheet membrane	(a) NIPS with mixtures of water/DMAc as coagulation baths; (b) VIPS	No	(a) CA: 114–141.5°; SA: N.A. (b) CA:144–150.6°; SA: N.A.	N.A.
[23]	PVDF flat sheet membrane	VIPS	No	CA: 91–136.3°; SA: N.A.	DCMD
[26]	PVDF hollow fiber membrane	NIPS with mixture of water and isopropanol as coagulation bath	Teflon® AF 2400 coating	CA: 140–151°; SA: N.A.	DCMD
[20]	PVDF-HFP nanofibrous membrane	Electrospinning with incorporation of carbon nanotubes	No	CA: 151.4–158.5° SA: N.A.	DCMD
[29]	PVDF nanofibrous membrane	Electrospinning	CF4 plasma treatment	CA: 140.8–160.9°; SA: 51 – 52°	AGMD
[14]	Polysulfone nanofibrous membrane	Electrospinning	Poly-dimethylsiloxane (PDMS) coating and cold-press posttreatment	CA: 141.7–153.9°; SA: N.A.	DCMD
[8]	Polyimide nanofibrous membrane	Electrospinning	P-phenylenediamine and 1H, 1H, 2H, 2H-perfluorodecanethiol coating	CA: 143.5–155.1°; SA: ~ 6.5°	Oil–water separation
This work	PVDF flat sheet membranes	Spray-assisted nonsolvent induced phase separation (SANIPS)	No	CA: 151.9–156.2°; SA: 9.6–22.6°	DCMD

nanofibrous membranes still require addition of nanomaterials or other modifications in order to achieve superhydrophobicity[8,14,20,29].

Besides generating hierarchical surface structures with multi-level roughnesses, it is often necessary to lower surface energy in order to achieve superhydrophobicity. Fluorinated materials, including fluorine-containing plasma gases, Teflon™ amorphous fluoroplastics, fluorographite, and fluoroalkylsilane, are most commonly applied because of their low surface energies and remarkable water repellences[29,31–34]. However, their relatively high cost and poor biodegradability impede the application on a wider and larger scale.

In this work, we present a facile and green method to fabricate superhydrophobic PVDF membranes via spray-assisted nonsolvent induced phase separation (SANIPS). Spraying is adopted to manipulate the morphology of semicrystalline polymer membranes by controlling the phase inversion speed and crystallization growth rate. The method does not require any further posttreatment and uses water as the sole coagulation medium. We have revealed the underlying mechanisms and systematically investigated effects of key parameters in this SANIPS method. The superhydrophobicity and self-cleaning ability of the resultant superhydrophobic membranes have been tested under direct contact membrane distillation (DCMD) mode with high-salinity dye wastewater as the feed solution. Last but not least, universally applying the SANIPS method to fabricate highly porous and hierarchical surface structures has been validated, using other commercially available semicrystalline polymeric materials, such as poly(vinylidene fluoride-co-hexafluoropropylene) (PVDF-HFP) and polyacrylonitrile (PAN).

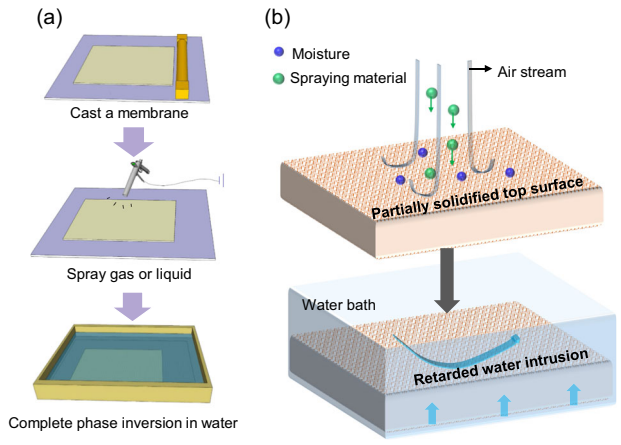

Fig. 1 The SANIPS method. a Schematic diagram and **b** proposed mechanism of the SANIPS method.

RESULTS

Superhydrophobic and self-cleaning properties of resultant membranes

Flat sheet polymer membranes were prepared via the SANIPS method as illustrated in Fig. 1a. Membranes were named as SANIPS-A, SANIPS-E, and SANIPS-W, corresponding to air, ethanol, and water as the spraying materials, respectively. A control membrane (NIPS) without spraying treatment was also prepared for comparison (Supplementary Table 1). In contrast to the small

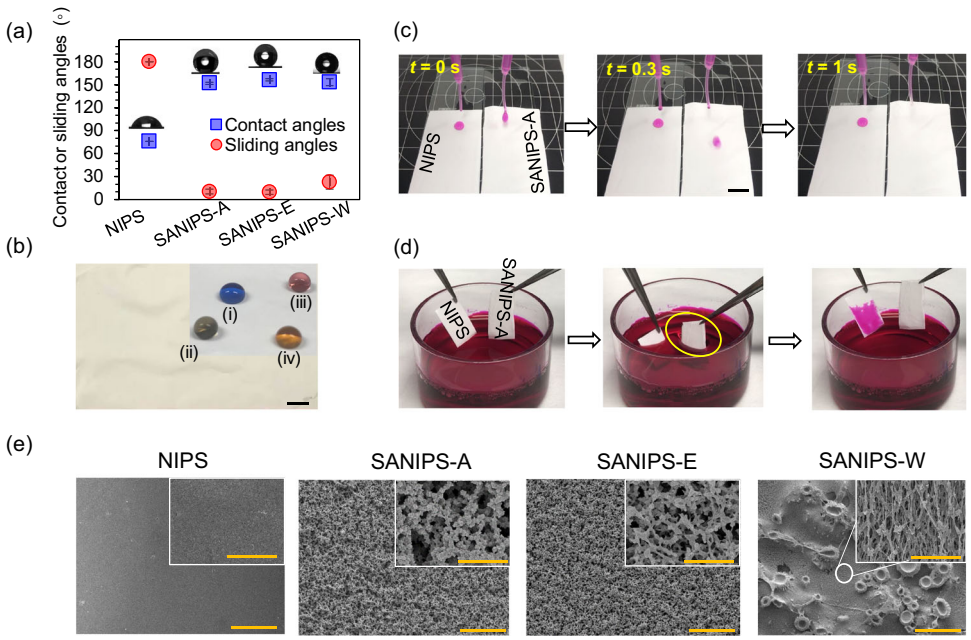

Fig. 2 Surface hydrophobicity and morphological structures. a Water contact and sliding angles on different membranes. Error bars present standard deviations. **b** A picture of air-treated SANIPS membrane (SANIPS-A) with an area of 11.5 cm × 8 cm. The inserted image shows droplets of (**i**) 0.2 mM SDS and (**ii**) 2000 p.p.m. GO aqueous solution, (**iii**) Rose Bengal dyed water, and (**iv**) 1:9 ethanol/water mixture on the membrane top surface; scale bar: 1 cm. **c** Pictures of dropping Rose Bengal dyed water droplets on SANIPS-A and nonsolvent induced phase separation (NIPS) from 0 to 1 s. Membranes were tilted at an angle of 10°; scale bar: 1 cm. **d** Self-cleaning test of NIPS and SANIPS-A by immersing the membranes in a Rose Bengal dye solution. Dye concentration in **c** and **d** is 1 wt%. **e** FESEM images of top surfaces of NIPS and SANIPS membranes; scale bar: 50 μm. Inserted FESEM images are enlarged pictures of membrane top surfaces; scale bar: 5 μm.

water contact angle of the control NIPS membrane (75.8°), all the SANIPS membranes exhibit water contact angles over 150° (Fig. 2a). Besides pure water, SANIPS membranes also show great repellence toward various types of aqueous solutions that contain 0.2 mM sodium dodecyl sulfate (SDS), 1% Rose Bengal, 2000 p.p.m. graphene oxide (GO), or 10% ethanol (Fig. 2b), indicating their potential for wide applications in the field of wastewater treatment. Figure 2c and Supplementary Video 1 record the movement of a water droplet on the tilted NIPS and SANIPS-A membranes. The water droplet rapidly rolls off from SANIPS-A, while it remains adhered to the NIPS membrane. In fact, the water droplet will not come off even when the NIPS membrane is turned upside down. The self-cleaning properties of different membranes are assessed by immersing them in a Rose Bengal aqueous solution of 1 wt%. As shown in Fig. 2d, Supplementary Fig. 1, and Supplementary Video 2, the water surface is distorted downward when SANIPS membranes are immersed in water, as a result of the strong water repellency of the superhydrophobic surface. When being taken out from the dye solutions, all the SANIPS membranes remain unstained, contrasting sharply with the control NIPS membrane.

Figure 2e and Supplementary Fig. 2a compare the surface morphologies, and topologies of NIPS and SANIPS membranes. Different from the smooth surface of the NIPS membrane, surfaces of all SANIPS membranes feature hierarchically structures and high surface porosities (Table 2). It is widely accepted that a liquid droplet stays in a Cassie–Baxter state on a superhydrophobic surface, where the liquid is retained on the liquid–solid–vapor interface, and wetting is prevented by air pockets trapped between the solid and liquid phases[10,35]. The apparent contact angle θ^* is given by the Cassie–Baxter relationship $\cos\theta^* = -1 + f_s(1 + \cos\theta)$, where θ is the equilibrium contact angle and f_s is the wetted area of the solid–liquid interface on a projected area of unity[36,37]. The equation highlights the importance of minimizing the solid fraction at the contacting surface between membrane and water. Therefore, high surface porosity and roughness are beneficial to achieve a large water contact angle. In addition, the significance of multilevel roughness in improving the robustness of the Cassie–Baxter state has been emphasized by many scholars[36]. Consequently, the SANIPS membranes exhibit much superior water repellence to the smooth NIPS membrane. On the other hand, Fig. 2e and Supplementary Fig. 2a also show that different spray materials result in distinct surface morphologies and topologies. The special role of spraying during the phase inversion process and the effects of different spray materials on membrane properties will be elucidated in the following discussions.

Effects of air spray

As shown in Fig. 2e and Supplementary Fig. 2, the control NIPS membrane exhibits an asymmetric structure with a relatively smooth and dense top surface, and a cross section with cellular structure and figure-like macrovoids, which can be ascribed to rapid liquid–liquid demixing using a strong nonsolvent (i.e., water) as the coagulant medium[25,38–40]. However, even though the SANIPS-A membrane was also subsequently precipitated in a water bath after the air spraying, it possesses a highly porous top surface with a multilevel roughness and a symmetrical macrovoid-free sponge-like cross section. In general, macrovoids are undesirable as they are mechanically weak points that may facilitate pore wetting and lead to membrane failure in the long run[41].

To investigate the effects of air spraying on membrane formation, we took the picture of the nascent membrane immediately after it was treated by the compressed air before being submerged in water and compared it with the newly cast control membrane. As shown in Fig. 3a, air spraying turns the original mirror-like surface with specular reflection to a frosted surface with diffuse reflection, indicating the occurrence of surface solidification. The nascent membrane samples were also observed using a polarized light microscope (PLM), which is a common tool

Table 2. A summary of surface porosity, and surface pore sizes of NIPS and SANIPS membranes.

Surface properties	NIPS	SANIPS-A	SANIPS-E	SANIPS-W
Surface porosity (%)	5.6 ± 0.2	54.4 ± 0.1	47.6 ± 0.2	34.5 ± 0.1
Mean pore size (nm)	4.4 ± 0.1	227.3 ± 45.7	221.0 ± 22.5	168.4 ± 13.4
Min pore size (nm)	2.0 ± 0.0	30.3 ± 7.7	25.4 ± 5.2	21.3 ± 3.4
Max pore size (nm)	31.2 ± 0.7	6290.4 ± 206.8	4069.3 ± 126.5	1156.4 ± 58.7

to monitor phase inversion during the formation of polymeric membranes[27,42]. As shown in Fig. 3b, the control membrane remains transparent in air, while the air-treated one shows microscale fine corrugations on the membrane surface, reaffirming that phase inversion occurs during the air spraying process.

The rapid phase inversion of SANIPS-A may be attributed to the combined effects of several factors. First, the compressed air flow causes convective cooling and reduces the surface temperature of the thin film. In the meantime, moisture condensation is accelerated due to the rapid cooling, resulting in a fast phase inversion at the membrane surface. To verify our speculation, mass changes of NIPS and SANIPS-A nascent membranes in air have been closely monitored, and Fig. 3c shows the normalized results as a function of time. Mass of the control NIPS membrane increases at a relatively constant rate of ~0.0042% per second in the first 120 s due to the continuous absorption of moisture in air. Mass of SANIPS-A, by contrast, increases drastically by 0.67% immediately after the air spraying, which evidences that moisture condensation is significantly accelerated. Interestingly, after the air spraying is terminated, the mass increasing rate of SANIPS-A quickly drops to 0.003% per second, even lower than that of NIPS. This can be ascribed to the partial solidification of the top surface that impedes the subsequent solvent evaporation and moisture diffusion.

On the other hand, the effect of air spraying is more than simply accelerating the phase inversion process. To elucidate this point, we compared the SANIPS-A with membranes prepared via VIPS (Supplementary Table 2). Supplementary Fig. 3 shows that hierarchical structures and superhydrophobicity cannot be achieved even with a prolonged exposure duration of 30 min. Therefore, we conclude that the spraying process contributes more than simply expediting the phase inversion. The turbulent compressed air stream also causes local distortion of membrane surface, which plays a critical role in the formation of hierarchical roughness.

After air spraying, the nascent membrane is transferred to a water coagulant bath to complete the phase inversion. Different from the NIPS method where solvent and nonsolvent exchange rapidly at the membrane–water interface, the water in-flow and the *N*-methyl-2-pyrrolidone (NMP) out-flow in the nascent SANIPS-A membrane is greatly hindered by the newly formed top skin. Thus, a delayed demixing occurs that allows polymer crystals to grow and form a macrovoid-free cross section structure full of spherulitic globules. The mechanism of the SANIPS process has been illustrated in Fig. 1b.

Effects of different spraying materials

After understanding the specific roles of air spraying in the phase inversion progress, we studied the effects of different spray materials on membrane formation. Ethanol and water were selected because of their low costs and low toxicity. In addition, they have different physicochemical properties as tabulated in Supplementary Table 3 (ref. [25]). Figure 2e shows the surface morphological images of the membrane treated by ethanol spraying (SANIPS-E), which has a uniform open structure and multilevel coralloidal morphology. By contrast, the water-treated membrane (SANIPS-W) reveals distinct volcano structures on its relatively less porous top surface. Topological images (Supplementary Fig. 2a) and roughness data (Fig. 4a) disclose an interesting phenomenon. With a large scan size of 60 μm × 60 μm, the roughness increases in the order of SANIPS-A < SANIPS-E < SANIPS-W, while this trend reverses on a smaller scan area of 10 μm × 10 μm. The former trend can be attributed to the formation of different microscale structures. As shown in Fig. 2e, the microscale structure of SANIPS-A is constituted by clusters of nanoscale polymer crystals. However, for SANIPS-E and SANIPS-W, the bombardment of liquid droplets causes the formation of large ridges separated by wide valleys (Fig. 2e, Supplementary Fig. 2a), resulting in their higher roughnesses. At a smaller scan size, the instrument focuses on the nano-level structures and the valleys of SANIPS-E and SANIPS-W. The transition from the expanded spherulitic crystal structure to a flatter network structure corresponds to the decrease in roughness in the order of SANIPS-A > SANIPS-E > SANIPS-W.

As compared to air spraying, the introduction of liquid nonsolvents as the spraying materials cause more rapid solvent–nonsolvent exchange, thus inducing faster phase inversion at dope-liquid contacting spots[43]. The size of liquid droplets depends largely on the intermolecular attraction. Ethanol, which has a weak intermolecular force as indicated by its low surface tension of 21.97 mN m^{-1} at 25 °C (ref. [44]), can form a finer mist than water[45]. As shown in Fig. 3b, a relatively uniform phase separation is achieved on the membrane surface after ethanol spraying. Nevertheless, several dark spots can be observed possibly due to the collision of ethanol droplets and the resulted nuclei agglomeration of phase-inversed polymer chains, which later grows into microscale humps (Supplementary Fig. 2a). On the other hand, the PLM image of SANIPS-E shows opaquer than SANIPS-A (Fig. 3b), implying a more rapid phase inversion after ethanol spraying. This is because the evaporation of ethanol leads to a lower temperature at the membrane surface and facilitates the top skin formation, leaving a shorter time for the polymer crystals to grow. Therefore, SANIPS-E exhibits a less rough coralloidal structure on the nanoscale as compared to SANIPS-A as shown in Fig. 2e.

Water, however, possesses a high surface tension of 71.99 mN m^{-1} at 25 °C due to the strong hydrogen bonding[44]. As a result, the water mist contains larger droplets than those in the ethanol mist. In other words, with the same amount of spraying materials, there are fewer water droplets than ethanol droplets. A comparison of PLM images between SANIPS-E and SANIPS-W (Fig. 3b) confirms our hypothesis because the phase inversion spots in SANIPS-W are much less than SANIPS-E. Moreover, the difference in solubility parameter between water and PVDF is much greater than that between ethanol and PVDF (i.e., 24.6 vs. 3.3 $MPa^{1/2}$)[25,27], which makes water a far stronger nonsolvent than ethanol toward PVDF. Thus, when water droplets hit the nascent membrane, a drastic phase separation occurs immediately at the contact points, creating volcano structures as exhibited in Fig. 2e and Supplementary Fig. 2b. When the membrane is submerged in a water bath, liquid–liquid demixing takes place at the interface between water and the unsolidified polymer solution. As a result, a morphology consisting of volcanos and a relatively less porous skin is formed. Interestingly, among SANIPS-A, SANIPS-E, and

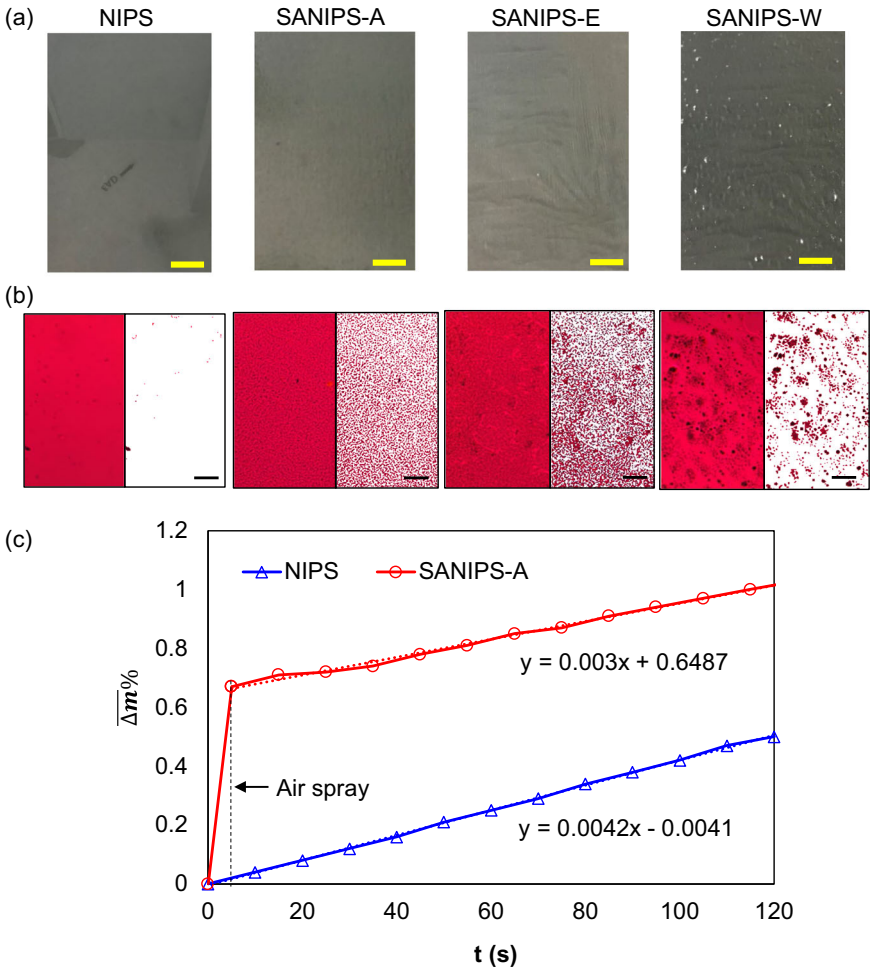

Fig. 3 Nascent membranes in air. a Pictures of nascent membranes in air; scale bars: 2 cm. **b** PLM images (left) and ImageJ enhanced PLM images (right) of top surfaces of nascent membranes in air; scale bars: 100 μm. **c** Water absorption rates of NIPS and SANIPS-A in humid air.

SANIPS-W, the SANIPS-W membrane has the thinnest wall thickness (Fig. 4b). This arises from the fact that it has the least porous top skin (Fig. 2e), which exerts the highest resistance for water intrusion during the liquid–liquid demixing.

Consistent with the trend in the morphology, the SANIPS-W membrane has the highest tensile stress and Young's modulus among these three SANIPS membranes (Fig. 4c) due to its smallest surface porosity and pore size (Table 2), and highly interconnected cross-sectional structures (Supplementary Fig. 2b). Although SANIPS-A and SANIPS-E exhibit almost similar porosity, wall thickness and cross-sectional structures, the latter has higher tensile stress and Young's modulus than the former mainly due to the smaller surface porosity and pore size. Despite that MD operates at a mild pressure, membranes with greater mechanical integrities are still highly desirable because in the large-scale application a hydraulic pressure must be applied to counter-balance the pressure drop, which can be high when a high flow rate, or a long and congested module is used.

Figure 4d compares liquid entry pressure (LEP) of different membranes. Generally, LEP is the applied hydraulic pressure at which water can penetrate through the membrane. It is an important indicator of anti-wetting property for a membrane. Thanks to the remarkable water repellences, all the SANIPS membranes exhibit LEP values >2 bar. SANIPS-E even achieves a remarkable LEP of 3.58 bar, outperforming most existing DCMD membranes[18,46–48]. SANIPS-E has the highest LEP value because it has (1) the highest water contact angle (Fig. 2a), (2) smaller surface porosity and pore size than SANIPS-A (Table 2), and (3) unique reentrant surface structures and spherulitic cross-sectional structure that are essential for robust hydrophobicity[32,35,36]. The LEP measurement proves the superior anti-wetting abilities of SANIPS membranes.

DCMD tests

The wetting resistance and self-cleaning abilities of NIPS and SANIPS membranes have been further tested by treating a feed solution containing 2000 p.p.m. Rose Bengal and 10% sodium chloride (NaCl) via DCMD. As shown in Fig. 5a, NIPS experiences a gradual decrease in flux after 1 h, while all the SANIPS membranes maintain stable fluxes throughout the 5 h tests. Interestingly, despite the significant flux reduction, the rejection of NIPS is still >99.9% throughout the test. That implies the flux decline is mainly ascribed to surface wetting, and pore blockage by dye molecules and salt crystals. Thus, the rejection data are not displayed due to their negligible changes throughout the tests. Inserted images in Fig. 5a compare different membranes after DCMD tests. Red stains from Rose Bengal are clearly observed on NIPS, indicating a severe dye adsorption. On the contrary, all the SANIPS membranes remain clean due to their excellent self-cleaning abilities. Supplementary Fig. 4a compare the surface morphology between NIPS and SANIPS-W after DCMD tests, which verifies the superior self-cleaning ability of the SANIPS membrane to the traditional NIPS membrane.

DCMD tests show that SANIPS-E and SANIPS-W have slightly higher vapor fluxes than SANIPS-A. To further increase the fluxes,

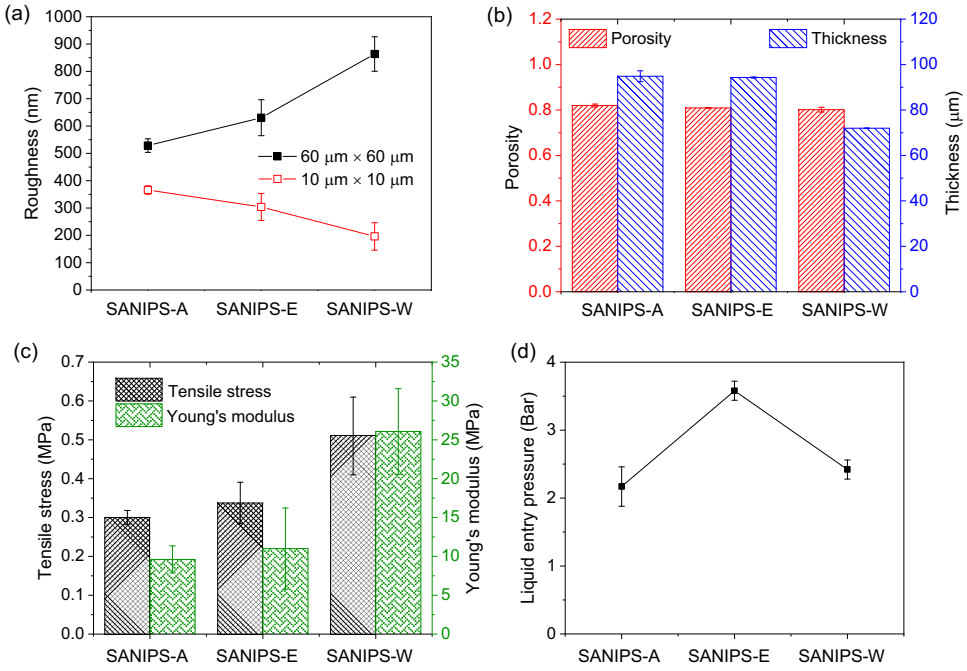

Fig. 4 Properties of SANIPS membranes. a Roughness of top surfaces, **b** porosity and thickness, **c** tensile stress and Young's modulus, and **d** liquid entry pressure of different SANIPS membranes. Error bars present standard deviations.

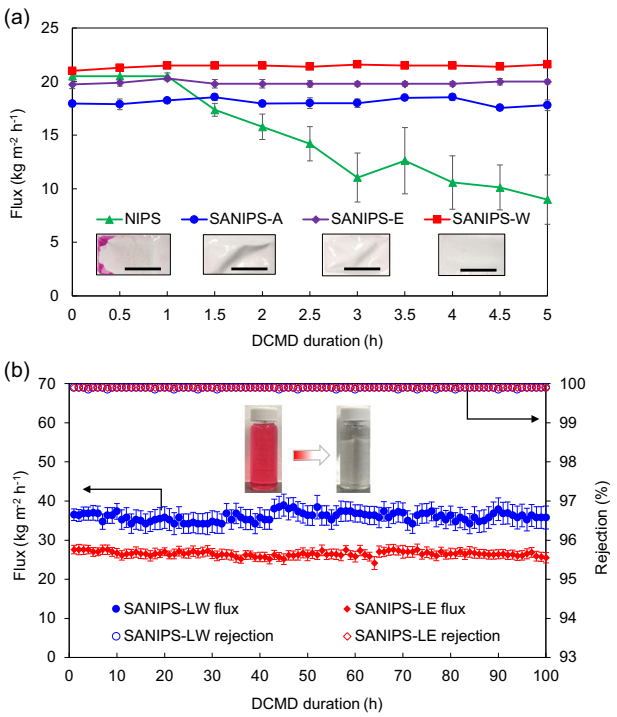

Fig. 5 DCMD tests. a Short-term DCMD fluxes of NIPS and SANIPS membranes. Inserted images are pictures of membrane top surfaces after the DCMD tests; scale bar: 1 cm. **b** Long-term DCMD performances of SANIPS-LE and SANIPS-LW. Inserted images are pictures of feed solution (left) and distillate (right). Error bars present standard deviations.

the PVDF concentration in the dope solutions was reduced by 3% to prepare SANIPS-LE and SANIPS-LW. As shown in Supplementary Fig. 4, both membranes exhibit multilevel roughness and remarkable superhydrophobicity. Their fluxes and wetting resistances were then tested in long-term DCMD processes to treat a feed solution containing 2000 p.p.m. Rose Bengal and 10% NaCl at 60 °C (Fig. 5b). The lower polymer concentration results in remarkable average fluxes of 26.5 and 36.0 kg m^{-2} h^{-1} for SANIPS-LE and SANIPS-LW, respectively. The flux of the latter is higher due to the thinner membrane thickness (Supplementary Fig. 4f). In addition, both membranes show stable performances and salt rejections over 99.9% throughout the entire 100 h tests, demonstrating their great potential in treating high-salinity dye wastewater. Consistent with the aforementioned LEP values, SANIPS-LE exhibits less flux fluctuations than SANIPS-LW.

Other commercial semicrystalline polymers

To explore the potential of using this SANIPS method for fabricating highly porous membranes with superhydrophobicity and multilevel roughness, PVDF-HFP and PAN membranes were prepared via NIPS and SANIPS methods (Supplementary Table 4). Compressed air and water, instead of ethanol, were employed as spraying materials to minimize the use of organic solvents. As shown in Fig. 6a, b, the SANIPS method significantly increases the surface roughness and porosity, and greatly suppresses the formation of macrovoids for both PVDF-HFP and PAN membranes. As a result, SANIPS PVDF-HFP membranes exhibit near superhydrophibicity and self-cleaning ability, as indicated by their large contact angles and small sliding angles (Fig. 6c). Surprisingly, the spraying treatment pulls down the contact angles of PAN membranes to a near superhydrophilic level (Fig. 6d). This is ascribed to the hydrophilic nature of PAN that favors a complete wet state (Wenzel state). As predicted by Wenzel's correlation: $\cos\theta^* = r\cos\theta$, where r is the roughness (i.e., the ratio of the total solid surface area to the projected area), the apparent contact angle decreases with the increase of roughness for a hydrophilic surface[36]. Similar to the enhancement in hydrophobicity, improving membrane hydrophilicity is also highly desirable in several membrane applications, such as ultrafiltration and microfiltration because a high hydrophilicity not only promotes water absorption and transfer, but also improves fouling resistance to organic contaminants[49,50]. Future research should aim to fine-tune the

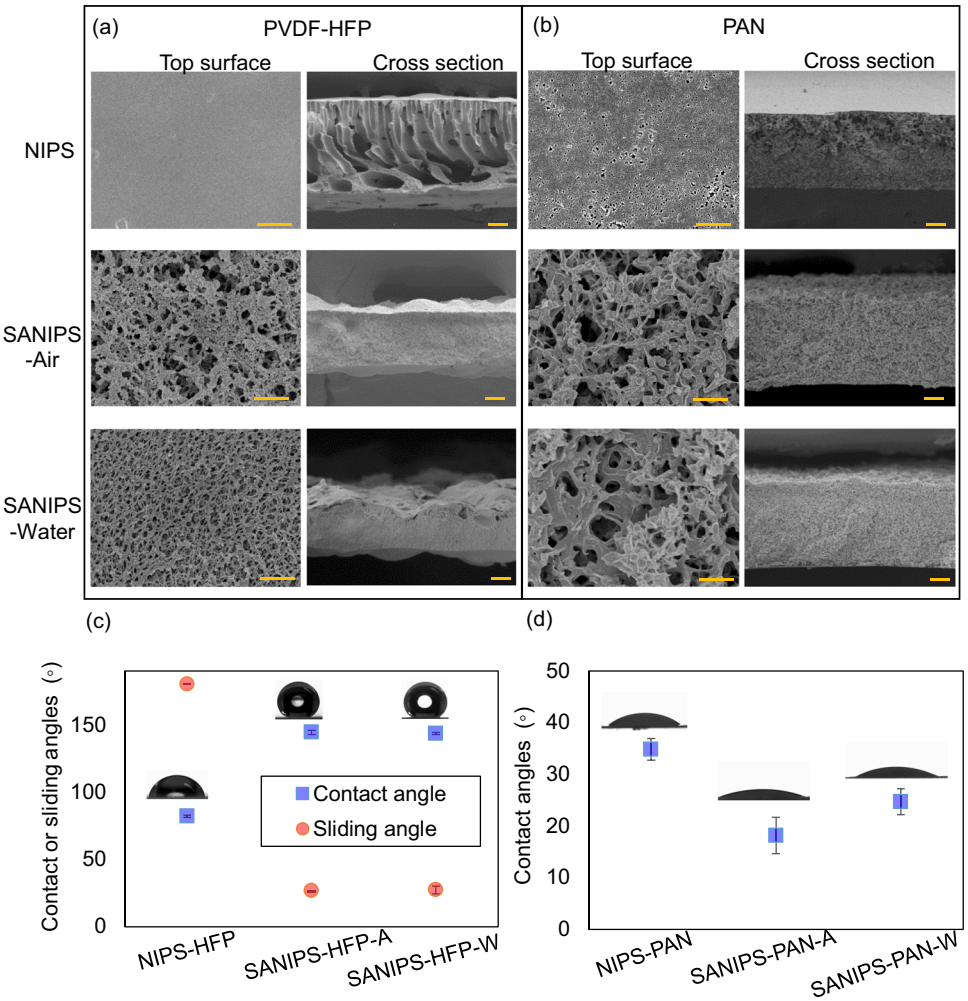

Fig. 6 PVDF-HFP and PAN membranes. FESEM images of top surfaces and cross sections **a** PVDF-HFP and **b** PAN membranes prepared via NIPS, SANIPS with air spraying and water spraying; scale bar for images of top surface and cross sections: 2 μm and 20 μm, respectively. **c** Contact and sliding angles of PVDF-HFP membranes. **d** Contact angles of PAN membrane. Error bars present standard deviations.

fabrication parameters to develop membranes with superhydrophobicity and superhydrophilicity for various applications.

DISCUSSIONS

This work introduces a SANIPS method to develop superhydrophobic and self-cleaning PVDF membranes, with high porosities and tunable multilevel roughnesses. We believe that the spraying step not only induces a rapid partial surface solidification but also causes local distortion of the membrane surface, and thus generates the first level roughness. Subsequently, when the nascent membrane is transferred into water coagulant, the newly formed skin will impede the solvent–nonsolvent exchange, and result in delayed demixing and the growth of second level roughness. In addition, membrane morphological structures can be tuned by applying different spraying materials. Materials with low surface tensions and solubility parameters, such as air and ethanol result in hierarchical spherulitic or coralloidal structures. On the opposite, water, a strong nonsolvent with a high surface tension, facilitates the formation of volcano-like humps on an open network structure.

Without any further surface modification, the SANIPS PVDF membranes exhibit superior repellence toward various types of aqueous solutions and show remarkable flux (36.0 kg m^{-2} h^{-1}), salt rejection (>99.9%), and long-term stability in treating feed solutions containing 10 wt% NaCl and 2000 p.p.m. Rose Bengal at 60 °C via DCMD. Moreover, we have demonstrated that the SANIPS method can be readily generalized to other semicrytalline polymers to significantly amplify their inherent hydrophobicity or hydrophilicity via increasing the surface roughness and porosity.

The SANIPS method provides a posttreatment-free and cost-effective way of designing porous membranes with superwettability. Additional degrees of freedom are introduced to the membrane fabrication as compared to the conventional NIPS and VIPS methods. In the SANIPS method, the phase inversion rate can be modulated by applying spraying materials with various physicochemical properties. Unlike in NIPS or VIPS where the nonsolvent takes either liquid or vapor form[22–24], spraying materials in SANIPS can be in the form of gas, liquid mixture, or even solid suspension. Moreover, the physical impact of the compressed flow causes local distortion of the membrane structure and introduces an extra level of roughness.

On the other hand, the study of the SANIPS method is still at an infant stage. Further studies should be conducted to investigate the effects of spraying parameters, such as the nozzle type and droplet size. Theoretical and experimental correlations connecting the spraying parameters and physicochemical interactions between the spraying materials and the dope systems to the

membrane structure and other properties should be established. With more future research, we are expecting extensive implementations of this method in both academia and industry to develop powerful membranes with super wetting properties for a wide range of applications.

MATERIALS AND METHODS

Materials

Commercial PVDF homopolymer (Kynar® HSV 900) and PVDF-HFP copolymer (Kynar Flex® 2801) were kindly provided by Arkema Inc. PAN ($M_w = 200{,}000$ g mol^{-1}) was acquired from Dolan GmbH. NMP (>99.5%), ethylene glycol (EG, > 99.5%), and NaCl (99.5%) were purchased from Merck. Ethanol (>99.98%) was ordered from VWR. Rose Bengal, methylene blue, and methyl orange were all acquired from Sigma Aldrich. GO solution (5 mg mL^{-1}) was purchased from Angstron Materials Inc. SDS was ordered from Thermofischer Scientific. All the above chemicals were used as received. Deionized (DI) water used in this work was produced by an Elga Option R7 unit.

Membrane preparation

PVDF (HSV900), NMP (solvent), and EG (nonsolvent) were added into a round-bottom flask and agitated at 60 °C overnight to obtain a transparent polymer blend. EG serves as a pore former to increase the membrane porosity, and it also acts as a nonsolvent that disturbs the equilibrium of the dope system and triggers the polymer precipitation[43]. Polymer solutions were then settled at 60 °C for 12 h to get rid of air bubbles. Flat sheet polymer membranes were prepared as illustrated in Fig. 1a. Firstly, the polymer solution was cast on a glass plate by a casting knife with a height of 200 µm. Subsequently, compressed air or a designated solution (~1 mL) was sprayed on the nascent membrane using an airbrush with a nozzle size of 0.3 mm for 30 s. The spraying duration of 30 s was selected based on the discussions in the Supporting Information. The air gun was moved over the glass plate at a constant speed of 5 cm s^{-1} to ensure a uniform spraying. If a liquid phase spraying material was applied, the membrane was sprayed by compressed air for another 5 s to facilitate the evaporation of the liquid solution. The airbrush was connected to a mini air compressor (HSENG AF18-2), which provided an average working pressure of 2 bar and an air flow rate of 20–23 L min^{-1}. The temperature and relative humidity of the ambient environment were 25 °C and 60%, respectively. The dope solution was maintained at 60 °C before the membrane fabrication. Next, the membrane was immersed and kept in DI water for 20 h to complete the phase inversion and then dried in a freeze dryer (S61-Modulyo-D, Thermo Electron Corp.) for future usage. These membranes are referred to as SANIPS PVDF membranes. Control membranes were prepared via the NIPS method, where the newly cast membrane was directly immersed in the coagulation bath of DI water for phase inversion. Dope compositions and fabrication conditions of SANIPS and NIPS membranes were summarized in Supplementary Table 1.

Characterizations

Surface morphology. Membrane morphology was observed by a field emission scanning electron microscope (FESEM JEOL JSM-7610F). To observe the cross-sectional structure, the sample was prepared by fracturing the membrane in liquid nitrogen. To monitor the degree of phase inversion in air, images of nascent membranes in air were taken before they were transferred to the water bath. Moreover, high-contrast microscopic images of nascent membrane surfaces in air were obtained by a PLM (Olympus SZX16 Stereomicroscope). The SANIPS membrane samples were firstly prepared by leveling a dope solution of 2 g on a glass slide (4.63 ± 0.01 g, 25 mm × 75 mm) using a blade, then air, ethanol, or water were sprayed on top of the sample surfaces for 2 s. PLM images were processed by ImageJ software (NIH) to remove the background and to further enhance the contrast.

Normalized mass change. The masses of small NIPS and SANIPS-A samples were monitored for 120 s by an accurate balance (A&D, GR-200). A total of 2 g of dope solution was levelled on a glass slide (4.63 ± 0.01 g, 25 mm × 75 mm) using a blade. Due to the viscous nature of the polymer solution, a small amount of it might adhere to the blade. Therefore, instead of taking 6.63 as the initial mass value, we recorded the actual total mass of the dope film and the glass as the initial mass value. The initial value of SANIPS-A was taken before the air spraying. During the 2 s of air spraying, no mass value was taken because the pressure of the compressed air may affect the balance reading. The second mass value was taken immediately after the spraying treatment. Subsequently, the mass of the sample was continuously recorded. Mass changes of different samples were normalized by the actual initial net mass of the polymer solution as described in Eq. (1):

$$\overline{\Delta m}\% = \left(\frac{m_t - m_i}{m_i - m_g}\right) \times 100\%, \quad (1)$$

where m_i (kg) and m_t (kg) were the sample masses at time zero and time t, respectively. m_g (kg) was the mass of the glass slide.

Surface topology and roughness. Surface topology was analyzed by Nanoscope III atomic force microscopy (Digital Instruments Inc.) with a tapping mode (Acoustic AC). To capture the roughness on both nanoscale and microscale, each sample was scanned with two scan sizes, namely, 10 µm × 10 µm and 60 µm × 60 µm. Since the obtained mean roughness (Ra) and root mean square roughness (Rq) have the same trends, only Ra was reported to avoid redundancy.

Membrane porosity. Membrane porosity was calculated based on the following equation:

$$\varepsilon = \left(1 - \frac{m_p}{\rho_p A \sigma}\right) \times 100, \quad (2)$$

where m_p (kg) was the mass of the polymer. Since the mass of air was negligible, m_p could be approximated by the mass of the dry membrane. A (m^2) and σ (m) were the effective area and the average thickness of the membrane. The membrane thickness was measured by examining its cross section using FESEM images. ρ_p was the density of the PVDF polymer.

The surface porosity and pore size were obtained by analyzing FESEM images of the membrane surfaces via ImageJ software (NIH). The results were summarized in Table 2.

Mechanical properties. Mechanical properties of membranes were analyzed by an Instron tensiometer (Model 3342, Instron Corp.). The starting gauge length, membrane width and elongation rate were set as 50 mm, 5 mm, and 10 mm min^{-1}, respectively. Five samples were tested for each condition and the average was obtained.

Contact and sliding angles. The dynamic water contact angles and sliding angles were measured with an optical contact angle measuring system (OCA25, Dataphysics) equipped with a tilting base unit. A DI water droplet with a volume of 6 µL was deposited on the membrane surface at a dispense rate of 2 µL s^{-1}. Contact angle was determined by the static sessile drop method. To measure the sliding angle, the platform was tilted at a rate of 1 degree per second. The titling angle at which the water droplet started to roll off was recorded as the sliding angle. All the measurements were conducted at room temperature (~25 °C) with a relative humidity of 60%. Five samples were tested for each condition.

Liquid entry pressure. LEP values of membranes were also measured using a home-made setup as shown in Supplementary Fig. 5. In an LEP test, a membrane size of 3 cm × 3 cm was mounted between two chambers that were then clamped tightly together. The top chamber was filled with a NaCl solution of 10%, while the bottom one was empty. Before the test, the top chamber was connected to compressed nitrogen, and then the entire testing unit was submerged in a DI water bath. During the test, the pressure in the top chamber was regularly increased at a rate of 0.25 bar per 10 min by a control valve, and the conductivity of the water bath was closely monitored. Once a constant increase in conductivity was observed, the pressure was recorded as the LEP. Three tests were conducted for each membrane.

DCMD tests

DCMD tests were performed on a lab scale setup as shown in Supplementary Fig. 6. A membrane with an effective area of 2 cm^2 was assembled into a plastic module holder. During the test, a feed

solution containing 10 wt% NaCl and 2000 p.p.m. Rose Bengal was contacting the superhydrophobic top surface of the membrane, and it was circulated at a flow rate of 0.15 L min^{-1}. Cold DI water was circulated at 0.1 L min^{-1} on the other side to condense water vapor. The temperatures of feed and distillate were maintained at 60 ± 1.5 °C and 15 ± 1.8 °C, respectively. The system was allowed to stabilize for 1 h before the weight and conductivity of the distillate were continuously monitored. The flux (N_w) and rejection (β) of the membrane were calculated using Eqs. (3) and (4), respectively.

$$N_w = \frac{\Delta W}{At} \tag{3}$$

$$\beta = \left(1 - \frac{C_p}{C_f}\right) \times 100\%, \tag{4}$$

where ΔW (kg) was the mass change of the distillate over a time duration t (s). C_p and C_f (mol L^{-1}) were NaCl concentrations in the distillate and feed streams, respectively. C_p was calculated based on Eq. (5) by considering the dilution effect:

$$C_p = \frac{C_1 m_1 - C_0 m_0}{m_1 - m_0}, \tag{5}$$

where m_0 and m_1 were the initial and final masses of the distillate bath, respectively. C_0 and C_1 were the initial and final salt concentrations of the distillate stream, respectively, which could be calculated based on the conductivity.

Pictures of membrane surfaces were taken after the DCMD tests. If the membrane was partially wet, dye molecules would penetrate membrane pores and change the color of the membrane surface, which provided a qualitative way of observing the degree of surface wetting. However, for the NIPS membrane, the observation could be affected by the thin film of dye wastewater adhered to the membrane surface. Therefore, to supress the interference of the attached dye wastewater, the membrane was quickly rinsed in DI water for 1 s before the picture was taken. The same procedure was applied to all the membranes to keep consistent.

DATA AVAILABILITY

All data needed to evaluate the conclusion in this paper are presented in the paper and/or the Supplementary Materials. Additional data related to this paper may be requested from the authors.

Received: 12 March 2020; Accepted: 8 June 2020;
Published online: 25 June 2020

REFERENCES

1. Himma, N. F., Prasetya, N., Anisah, S. & Wenten, I. G. Superhydrophobic membrane: progress in preparation and its separation properties. *Rev. Chem. Eng.* **35**, 211–238 (2019).
2. Wei, X. et al. CF 4 plasma surface modification of asymmetric hydrophilic polyethersulfone membranes for direct contact membrane distillation. *J. Memb. Sci.* **407–408**, 164–175 (2012).
3. Lee, E. J., Deka, B. J. & An, A. K. Reinforced superhydrophobic membrane coated with aerogel-assisted polymeric microspheres for membrane distillation. *J. Memb. Sci.* **573**, 570–578 (2019).
4. Li, J., Wang, N., Yan, H., Ji, S. & Zhang, G. Designing superhydrophobic surfaces with SAM modification on hierarchical ZIF-8/polymer hybrid membranes for efficient bioalcohol pervaporation. *RSC Adv.* **4**, 59750–59753 (2014).
5. Yu, X., An, L., Yang, J., Tu, S. T. & Yan, J. CO2 capture using a superhydrophobic ceramic membrane contactor. *J. Memb. Sci.* **496**, 1–12 (2015).
6. Zhang, W. et al. Superhydrophobic and superoleophilic PVDF membranes for effective separation of water-in-oil emulsions with high flux. *Adv. Mater.* **25**, 2071–2076 (2013).
7. Ke, Q., Jin, Y., Jiang, P. & Yu, J. Oil/water separation performances of superhydrophobic and superoleophilic sponges. *Langmuir* **30**, 13137–13142 (2014).
8. Ma, W. et al. Durable superhydrophobic and superoleophilic electrospun nanofibrous membrane for oil-water emulsion separation. *J. Colloid Interface Sci.* **532**, 12–23 (2018).
9. Khayet, M. Membranes and theoretical modeling of membrane distillation: a review. *Adv. Colloid Interface Sci.* **164**, 56–88 (2011).
10. Wang, W. et al. Trade-off in membrane distillation with monolithic omniphobic membranes. *Nat. Commun.* **10**, 3220 (2019).
11. Politano, A. et al. Photothermal membrane distillation for seawater desalination. *Adv. Mater.* **29**, 1–6 (2017).
12. Lu, K. J. & Chung, T. S. *Membrane Distillation: Membranes, Hybrid Systems and Pilot Studies*. (CRC Press, 2020).
13. Rezaei, M. et al. Wetting phenomena in membrane distillation: mechanisms, reversal, and prevention. *Water Res.* **139**, 329–352 (2018).
14. Li, X., García-Payo, M. C., Khayet, M., Wang, M. & Wang, X. Superhydrophobic polysulfone/polydimethylsiloxane electrospun nanofibrous membranes for water desalination by direct contact membrane distillation. *J. Memb. Sci.* **542**, 308–319 (2017).
15. Xu, N. et al. A water lily–inspired hierarchical design for stable and efficient solar evaporation of high-salinity brine. *Sci. Adv.* **5**, 1–8 (2019).
16. Verho, T. et al. Mechanically durable superhydrophobic surfaces. *Adv. Mater.* **23**, 673–678 (2011).
17. Meng, S., Mansouri, J., Ye, Y. & Chen, V. Effect of templating agents on the properties and membrane distillation performance of TiO2-coated PVDF membranes. *J. Memb. Sci.* **450**, 48–59 (2014).
18. Razmjou, A., Arifin, E., Dong, G., Mansouri, J. & Chen, V. Superhydrophobic modification of TiO2 nanocomposite PVDF membranes for applications in membrane distillation. *J. Memb. Sci.* **415–416**, 850–863 (2012).
19. Dong, Z.-Q., Ma, X.-H., Xu, Z.-L. & Gu, Z.-Y. Superhydrophobic modification of PVDF–SiO_2 electrospun nanofiber membranes for vacuum membrane distillation. *RSC Adv.* **5**, 67962–67970 (2015).
20. Tijing, L. D. et al. Superhydrophobic nanofiber membrane containing carbon nanotubes for high-performance direct contact membrane distillation. *J. Memb. Sci.* **502**, 158–170 (2016).
21. Sharifi, S. et al. Toxicity of nanomaterials. *Chem. Soc. Rev.* **41**, 2323–2343 (2012).
22. Peng, M. et al. Porous poly(vinylidene fluoride) membrane with highly hydrophobic surface. *J. Appl. Polym. Sci.* **98**, 1358–1363 (2005).
23. Al Marzooqi, F. A., Bilad, M. R. & Arafat, H. A. Improving liquid entry pressure of polyvinylidene fluoride (PVDF) membranes by exploiting the role of fabrication parameters in vapor-induced phase separation VIPS and non-solvent-induced phase separation (NIPS) processes. *Appl. Sci.* **7**, 1–15 (2017).
24. Kuo, C. Y., Lin, H. N., Tsai, H. A., Wang, D. M. & Lai, J. Y. Fabrication of a high hydrophobic PVDF membrane via nonsolvent induced phase separation. *Desalination* **233**, 40–47 (2008).
25. Sukitpaneenit, P. & Chung, T. S. Molecular elucidation of morphology and mechanical properties of PVDF hollow fiber membranes from aspects of phase inversion, crystallization and rheology. *J. Memb. Sci.* **340**, 192–205 (2009).
26. Lu, K. J., Zuo, J. & Chung, T. S. Tri-bore PVDF hollow fibers with a superhydrophobic coating for membrane distillation. *J. Memb. Sci.* **514**, 165–175 (2016).
27. Chang, J., Zuo, J., Zhang, L., O'Brien, G. S. & Chung, T. S. Using green solvent, triethyl phosphate (TEP), to fabricate highly porous PVDF hollow fiber membranes for membrane distillation. *J. Memb. Sci.* **539**, 295–304 (2017).
28. Khare, V. P., Greenberg, A. R. & Krantz, W. B. Vapor-induced phase separation - effect of the humid air exposure step on membrane morphology: Part I. Insights from mathematical modeling. *J. Memb. Sci.* **258**, 140–156 (2005).
29. Woo, Y. C. et al. CF4 plasma-modified omniphobic electrospun nanofiber membrane for produced water brine treatment by membrane distillation. *J. Memb. Sci.* **529**, 234–242 (2017).
30. Ma, M., Hill, R. M., Lowery, J. L., Fridrikh, S. V. & Rutledge, G. C. Electrospun poly (styrene-block-dimethylsiloxane) block copolymer fibers exhibiting superhydrophobicity. *Langmuir* **21**, 5549–5554 (2005).
31. Zhao, D., Zuo, J., Lu, K. J. & Chung, T. S. Fluorographite modified PVDF membranes for seawater desalination via direct contact membrane distillation. *Desalination* **413**, 119–126 (2017).
32. Chen, Y., Lu, K. J. & Chung, T. S. An omniphobic slippery membrane with simultaneous anti-wetting and anti-scaling properties for robust membrane distillation. *J. Memb. Sci.* **595**, 1–10 (2020).
33. Kota, A. K., Kwon, G. & Tuteja, A. The design and applications of superomniphobic surfaces. *NPG Asia Mater.* **6**, 1–16 (2014).
34. Lin, S. et al. Omniphobic membrane for robust membrane distillation. *Environ. Sci. Technol. Lett.* **1**, 443–447 (2014).
35. Tuteja, A., Choi, W., Mabry, J. M., McKinley, G. H. & Cohen, R. E. Robust omniphobic surfaces. *Proc. Natl Acad. Sci. USA* **105**, 18200–18205 (2008).
36. Lu, K. J., Chen, Y. & Chung, T. S. Design of omniphobic interfaces for membrane distillation – a review. *Water Res.* **162**, 64–77 (2019).
37. Lu, Y. et al. Robust self-cleaning surfaces that function when exposed to either air or oil. *Science* **347**, 1132–1135 (2015).
38. Smolders, C. A., Reuvers, A. J., Boom, R. M. & Wienk, I. M. Microstructures in phaseinversionmembranes. Part 1. Formation of macrovoids. *J. Membr. Sci.* **73**, 259–275 (1992).

39. Lin, D. J., Chang, C. L., Chen, T. C. & Cheng, L. P. On the structure of porous poly (vinylidene fluoride) membrane prepared by phase inversion from water-NMP-PVDF system. *Tamkang J. Sci. Eng.* **5**, 95–98 (2002).
40. Young, T. H., Cheng, L. P., Lin, D. J., Fane, L. & Chuang, W. Y. Mechanisms of PVDF membrane formation by immersion-precipitation in soft (1-octanol) and harsh (water) nonsolvents. *Polymer* **40**, 5315–5323 (1999).
41. Teoh, M. M. & Chung, T. S. Membrane distillation with hydrophobic macrovoid-free PVDF-PTFE hollow fiber membranes. *Sep. Purif. Technol.* **66**, 229–236 (2009).
42. Wang, L. Y., Yong, W. F., Yu, L. E. & Chung, T.-S. Design of high efficiency PVDF-PEG hollow fibers for air filtration of ultrafine particles. *J. Memb. Sci.* **535**, 342–349 (2017).
43. Zuo, J. In *Membrane Distillation: Membranes, Hybrid Systems and Pilot Studies* (eds Lu, K. J. & Chung, T. S.) 51–79 (CRC Press, 2020).
44. Lide, D. R. *CRC Handbook of Chemistry and Physics* (CRC Press, 2005).
45. Kooij, S., Sijs, R., Denn, M. M., Villermaux, E. & Bonn, D. What determines the drop size in sprays? *Phys. Rev. X* **8**, 31019 (2018).
46. Lu, X. et al. Amphiphobic PVDF composite membranes for anti-fouling direct contact membrane distillation. *J. Memb. Sci.* **505**, 61–69 (2016).
47. Lee, E. J., An, A. K., He, T., Woo, Y. C. & Shon, H. K. Electrospun nanofiber membranes incorporating fluorosilane-coated TiO 2 nanocomposite for direct contact membrane distillation. *J. Memb. Sci.* **520**, 145–154 (2016).
48. Wang, P., Teoh, M. M. & Chung, T. S. Morphological architecture of dual-layer hollow fiber for membrane distillation with higher desalination performance. *Water Res.* **45**, 5489–5500 (2011).
49. Liang, S. et al. Highly hydrophilic polyvinylidene fluoride (PVDF) ultrafiltration membranes via postfabrication grafting of surface-tailored silica nanoparticles. *ACS Appl. Mater. Interfaces* **5**, 6694–6703 (2013).
50. Goetz, L. A., Jalvo, B., Rosal, R. & Mathew, A. P. Superhydrophilic anti-fouling electrospun cellulose acetate membranes coated with chitin nanocrystals for water filtration. *J. Memb. Sci.* **510**, 238–248 (2016).

ACKNOWLEDGEMENTS

The authors would like to thank Dr. Susilo Japip, Dr. Sui Zhang, Dr. Liang Shen, Mr. Meng Li, and Mr. Marcus Wee Yong Low for their valuable advices and kind support. The authors would like to acknowledge the Singapore National Research Foundation, Prime Minister's Office, for supporting the project entitled, "Development of solvent resistant nanofiltration membranes for sustainable pharmaceutical and petrochemical manufacture" (CRP Award NRF-CRP14-2014-01 (NUS grant R-279-000-466-281)) under its Competitive Research Program.

AUTHOR CONTRIBUTIONS

K.J.L. and T.S.C. conceived the research. K.J.L. executed all the experiments and characterizations with partial assistance from D.Z., Y.C., and J.C. K.J.L. wrote the paper and all authors revised it.

COMPETING INTERESTS

The authors declare no competing interests.

ADDITIONAL INFORMATION

Supplementary information is available for this paper at https://doi.org/10.1038/s41545-020-0078-2.

Correspondence and requests for materials should be addressed to T.-S.C.

Reprints and permission information is available at http://www.nature.com/reprints

Publisher's note Springer Nature remains neutral with regard to jurisdictional claims in published maps and institutional affiliations.